Microelectronics Journal 111 (2021) 105041

Contents lists available at ScienceDirect

Microelectronics Journal

journal homepage: www.elsevier.com/locate/mejo

Ammonia optical gas sensing based on graphene-covered silicon microring resonators: A design space exploration

Wei Jia, Apratim Majumder, Sourangsu Banerji, Rajesh Menon, Berardi Sensale-Rodriguez [*]

Department of Electrical and Computer Engineering, The University of Utah, Salt Lake City, UT 84112, USA

ARTICLE INFO

Keywords:
Ammonia gas sensor
Microring resonator
Graphene
Waveguide modes

ABSTRACT

This paper discusses the design space exploration for an ammonia optical gas sensor based on a silicon microring resonator that is covered by graphene. A comparative analysis of the transmittance sensitivity of its fundamental quasi-TE and quasi-TM modes is presented. Results show that a large fraction of the fundamental quasi-TM mode's electrical energy is propagating outside the waveguide, which makes this geometry more sensitive to ammonia induced changes in Fermi energy of graphene. The overall transmittance intensity difference, for the fundamental quasi-TE mode is less than 1 dB, independent of ring radius, when the ammonia gas concentration is varied from 0.5 to 1000 ppm. For the fundamental quasi-TM mode, results show that a ring radius ~8.4 μm can provide critical coupling condition and lead to >20 dB modulation of transmittance intensity when the ammonia gas concentration is varied from 0.5 to 1000 ppm. Overall, proper selection of mode excitation as well as ring geometry is essential to attain practical sensitivity.

1. Introduction

Silicon photonics plays an increasingly important role in photonic integrated platforms due to its CMOS compatibility and high index contrast [1]. As an evolving technology, silicon photonics enables a small footprint of devices and large-scale integration [2]. Microring resonators are among the most intensively utilized components in silicon photonics and constitute an essential building block in integrated optical systems. Silicon microring resonators have been applied in lasers [3], electro-optical modulators [4,5], optical filters [6,7], and sensors [8,9]. Parallel to this evolution in Silicon photonics and microring resonator-based devices, the last decades have also witnessed a revolution in new photonic materials, with many of them being compatible with CMOS fabrication processes. In this context, graphene is a promising optical material whose interest has emerged during the last ten years. Graphene is a monolayer of carbon atoms arranged in a hexagonal lattice, and it has attracted broad research interest in optoelectronics devices due to its outstanding optical and electrical properties [10,11]. Graphene can absorb and interact with specific gas molecules. This results in a variation in its chemical potential. Therefore, the complex conductivity of graphene can be tuned when graphene is exposed to different chemicals. Individual gas molecules adsorbed on graphene can be detected through micrometer-sized sensors made from graphene [12]. Furthermore, by combining graphene with ring resonators, various types of applications have been proposed, such as wavelength routers in Photonic Network-on-Chip [13], high-speed photodetectors [14], and efficient graphene-silicon microring modulators [15]. Also, graphene-based ring resonators have been recently proposed for lab-on-a-chip label-free sensing [16].

This paper discusses the combination of silicon microring resonators with monolayer graphene to realize ammonia optical gas sensors. Although graphene is considered in this study, its derivatives such as graphene oxide or reduced graphene oxide could also be used for the analyzed optical gas sensor application. These materials might yield the advantage of not requiring surface functionalization, as is often the case in graphene, in order to attain selectivity to desired gases [17,18]. Silicon microring resonators can be made by using silicon-on-insulator (SOI) technology. The optical wavelength used here is in the communications band (1.55 μm). Although previous works have already tackled this application by focusing on the resonance wavelength shift as a mechanism to detect ammonia gas concentration [19], this approach requires high sensitivity of the measurement to detect a wavelength shift of less than 0.5 nm with a simultaneously very small change on transmission intensity. As shown in Ref. [19], the relative intensity difference for detecting ammonia gas concentration (when concentration is varied from 0.5 ppm to 1000 ppm) is less than 0.01, which can be easily buried in the

---

[*] Corresponding author.
E-mail address: berardi.sensale@utah.edu (B. Sensale-Rodriguez).

https://doi.org/10.1016/j.mejo.2021.105041
Received 25 November 2020; Received in revised form 22 February 2021; Accepted 15 March 2021
Available online 26 March 2021
0026-2692/© 2021 Elsevier Ltd. All rights reserved.

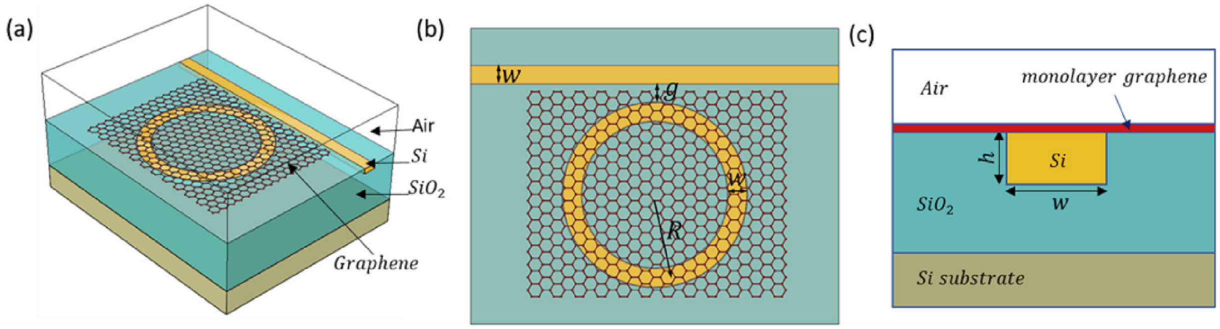

Fig. 1. (a) Proposed graphene silicon microring resonator, **(b)** the top view of the structure, and **(c)** the cross-section of the waveguide with $w = 500$ nm, $h = 220$ nm.

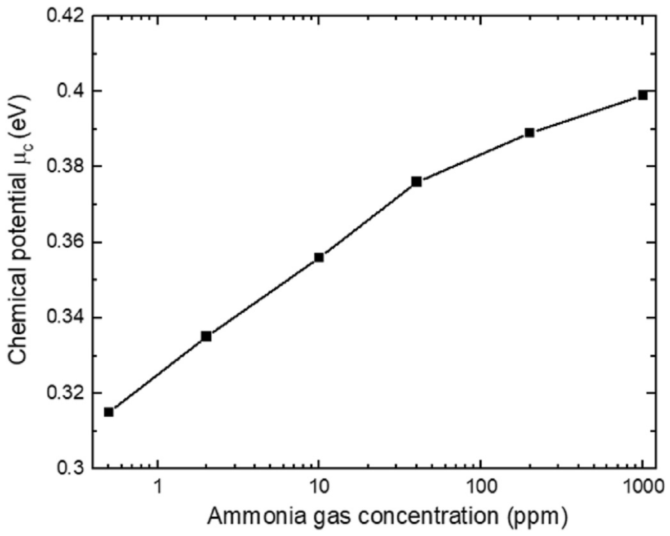

Fig. 2. Chemical potential μ_c of graphene with varied ammonia gas concentration from 0.5 ppm to 1000 ppm (data extracted from Ref. [19]).

background noise once performing measurements. Hence, in this work, we perform a careful design space exploration and focus on the transmittance intensity change of the microring resonator, rather than resonance wavelength shift, induced by varying ammonia gas concentration.

It is observed that transmittance intensity change, thus sensitivity, depends heavily on the ring waveguide radius and mode excitation. By choosing a proper ring radius and mode excitation, high transmittance sensitivity can be achieved. Compared to fundamental quasi-transverse electrical (TE) mode, fundamental quasi-transverse magnetic (TM) mode can induce high transmittance sensitivity (with a proper choice of ring waveguide radius). There are various existing ammonia sensing techniques, such as conducting polymer sensors [20], metal oxide-based sensors [21], and field-effect transistor sensors [22]; however, optical sensors such as those here proposed might provide advantages such as low power consumption and a small footprint [23].

2. Device structure

The proposed ammonia gas sensor structure consists of a straight bus waveguide and a ring waveguide. These are buried in silicon dioxide. A monolayer of graphene is placed on the waveguide's top surface, as illustrated in Fig. 1. The ring radius, *R*, is defined from the origin to the center of the ring waveguide. In our calculations, the ring radius is varied from 1 to 50 μm. The gap size between the straight waveguide and the ring waveguide is fixed to $g = 100$ nm. A 100 nm gap was selected since such dimensions can be easily achieved with standard fabrication processes. In general, the smallest the gap the larger the coupling coefficient. For larger gaps, the power coupled to the ring waveguide from the straight waveguide will be dramatically reduced, thus leading to a need for larger rings so as to achieve critical coupling. The whole device can be made on a silicon substrate using SOI technology. Due to the configuration of the device, the graphene can be easily transferred to the ring waveguide compared to the ridge waveguide configuration. The refractive indices employed in simulations for silicon and silicon dioxide are 3.477 and 1.444, at a wavelength of 1550 nm, respectively.

When the device is placed in an environment containing ammonia, the ammonia gas molecules interact with graphene. The absorbed ammonia gas molecules induce a change of Fermi level in the graphene

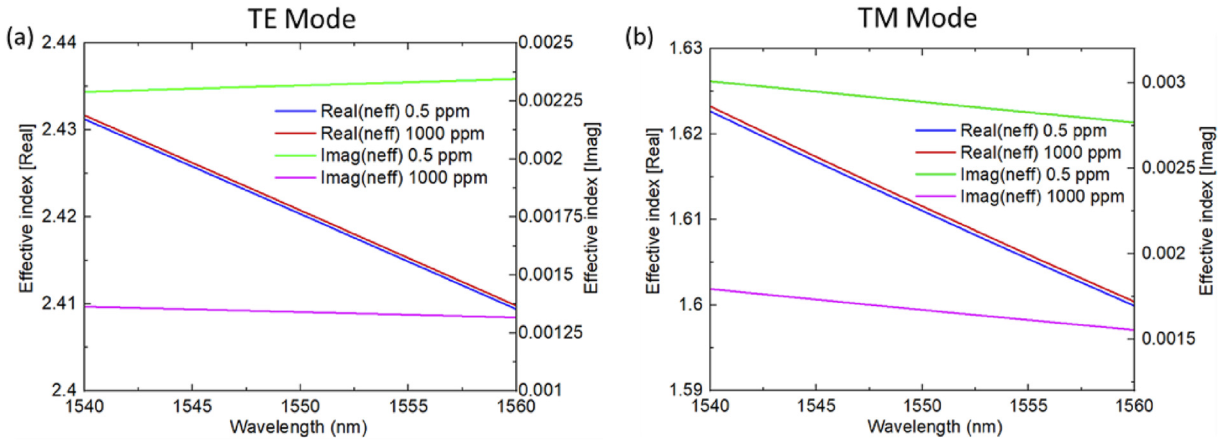

Fig. 3. Effective index of guided fundamental modes with ammonia gas concentration 0.5 ppm and 1000 ppm: **(a)** TE mode, **(b)** TM mode.

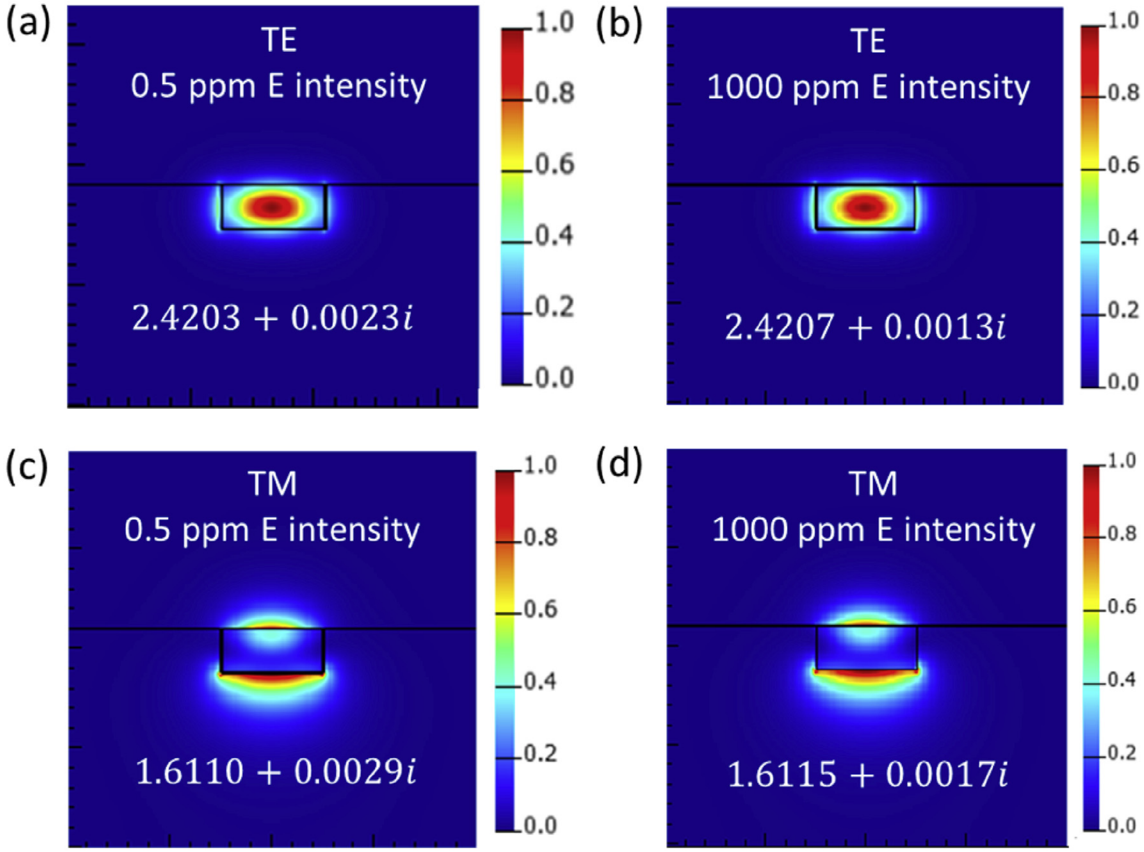

Fig. 4. Calculated electrical intensity distribution of fundamental quasi-TE and TM modes with ammonia concentration 0.5 ppm and 1000 ppm at 1550 nm: **(a)** TE mode under 0.5 ppm, **(b)** TE mode under 1000 ppm, **(c)** TM mode under 0.5 ppm, **(d)** TM mode under 1000 ppm.

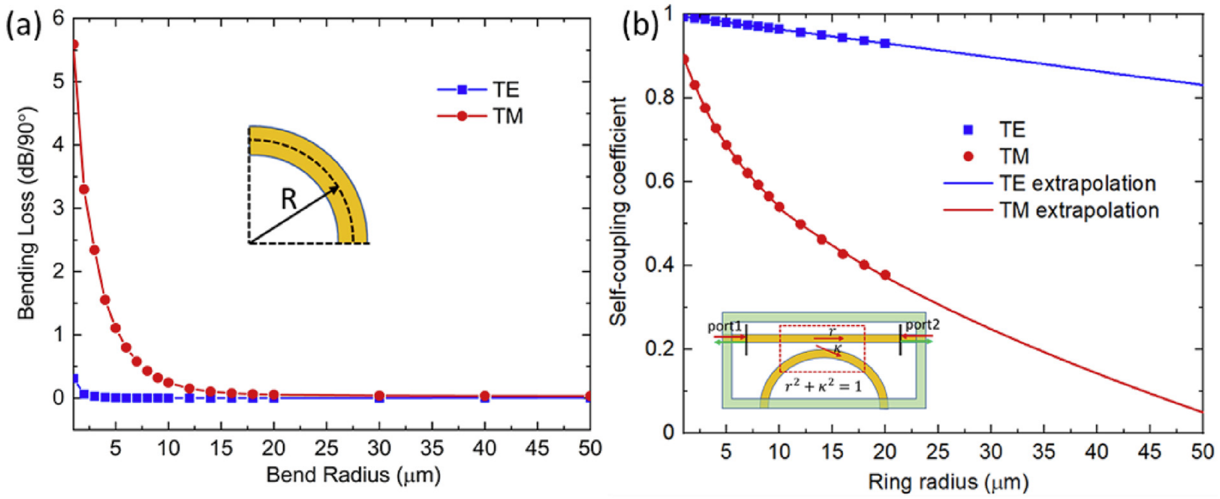

Fig. 5. (a) Bending loss as a function of the bend radius for the buried waveguide configuration. (**b)** Self-coupling coefficient, r, as a function of ring radius R.

layer, leading to a variation in its optical conductivity. The Fermi energy of the graphene layer varies based on the concentration of the ammonia gas molecules in the atmosphere.

3. Numerical modeling and results

The relative resistance change of graphene as a function of ammonia gas concentration in air was experimentally shown by Yavari et al. [24] From here, the relative conductivity can be calculated from the relative resistance change. The surface conductivity of single-layer graphene is given by Ref. [25]:

$$\sigma(\omega,\ \Gamma,\mu_c,T)=\sigma_{intra}(\omega,\ \Gamma,\mu_c,T)+\sigma_{inter}(\omega,\ \Gamma,\mu_c,T) \tag{1}$$

where ω is the angular frequency, Γ is the scattering rate, μ_c is the chemical potential, and T represents the temperature. In Eqn. (1), the intraband conductivity $\sigma_{intra}(\omega,\ \Gamma,\mu_c,T)$ is given by:

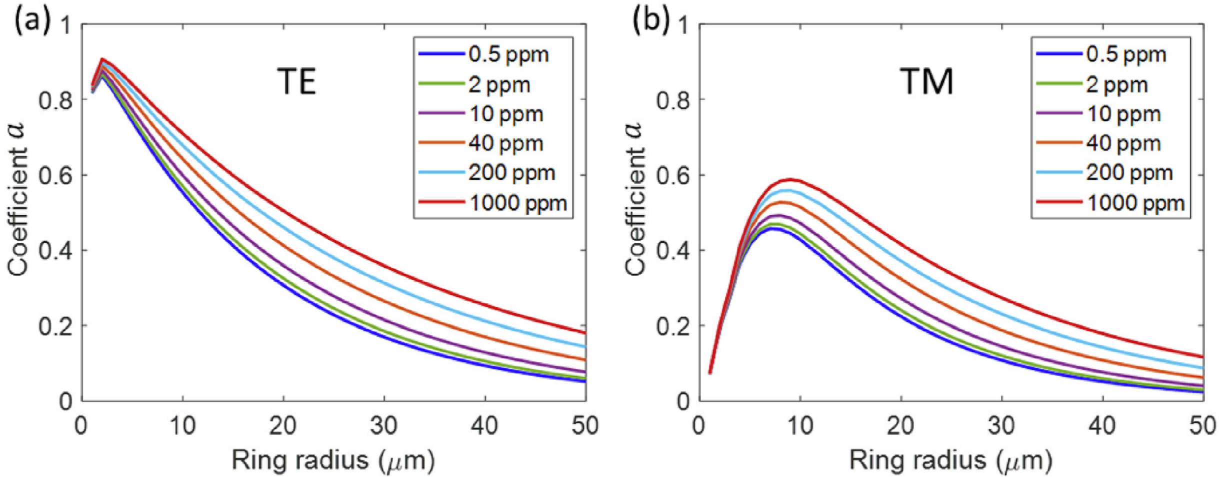

Fig. 6. Single pass amplitude transmission, *a*, under **(a)** fundamental quasi-TE mode, **(b)** fundamental quasi-TM mode.

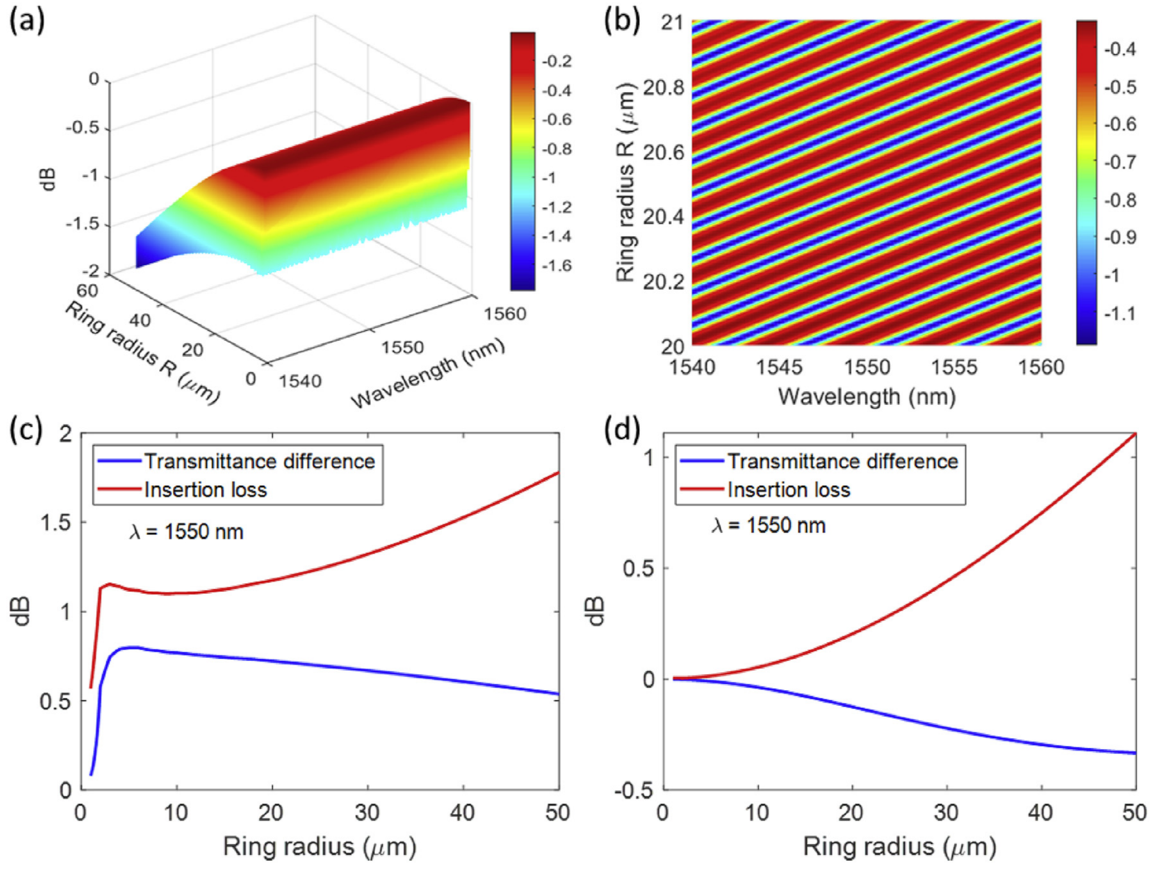

Fig. 7. Transmittance versus ring radius and wavelength under NH_3 gas concentration of 0.5 ppm **(a)** 3D surface plot, **(b)** detail on a 2D surface plot. Transmittance difference and insertion loss as a function of ring radius when the ammonia gas concentration is varied from 0.5 to 1000 ppm: **(c)** calculated from transmission minima, T_{min}, and **(d)** calculated from transmission maxima, T_{max}.

$$\sigma_{intra}(\omega,\ \Gamma,\mu_c,T)=\frac{-ie^2}{\pi\hbar^2(\omega+i2\Gamma)}\int_0^\infty \xi\left(\frac{\partial f_d(\xi)}{\partial\xi}-\frac{\partial f_d(-\xi)}{\partial\xi}\right)d\xi, \tag{2}$$

and the interband conductivity $\sigma_{inter}(\omega,\ \Gamma,\mu_c,T)$ is given by:

$$\sigma_{inter}(\omega,\ \Gamma,\mu_c,T)=\frac{ie^2(\omega+i2\Gamma)}{\pi\hbar^2}\int_0^\infty \frac{f_d(-\xi)-f_d(\xi)}{(\omega+i2\Gamma)^2-4(\xi/\hbar)^2}d\xi, \tag{3}$$

where $\hbar$ is reduced Planck's constant, k_B is Boltzman's constant, and $f_d(\xi)\equiv\left(e^{\frac{\xi-\mu_c}{k_BT}}+1\right)^{-1}$ is the Fermi-Dirac distribution.

The surface conductivity of graphene is generated by evaluating the σ_{inter} term numerically, and the σ_{intra} term analytically as following:

$$\sigma_{intra}(\omega,\ \Gamma,\mu_c,T)=i\frac{e^2k_BT}{\pi\hbar^2(\omega+i2\Gamma)}\left(\frac{\mu_c}{k_BT}+2\ln\left(e^{-\frac{\mu_c}{k_BT}}+1\right)\right), \tag{4}$$

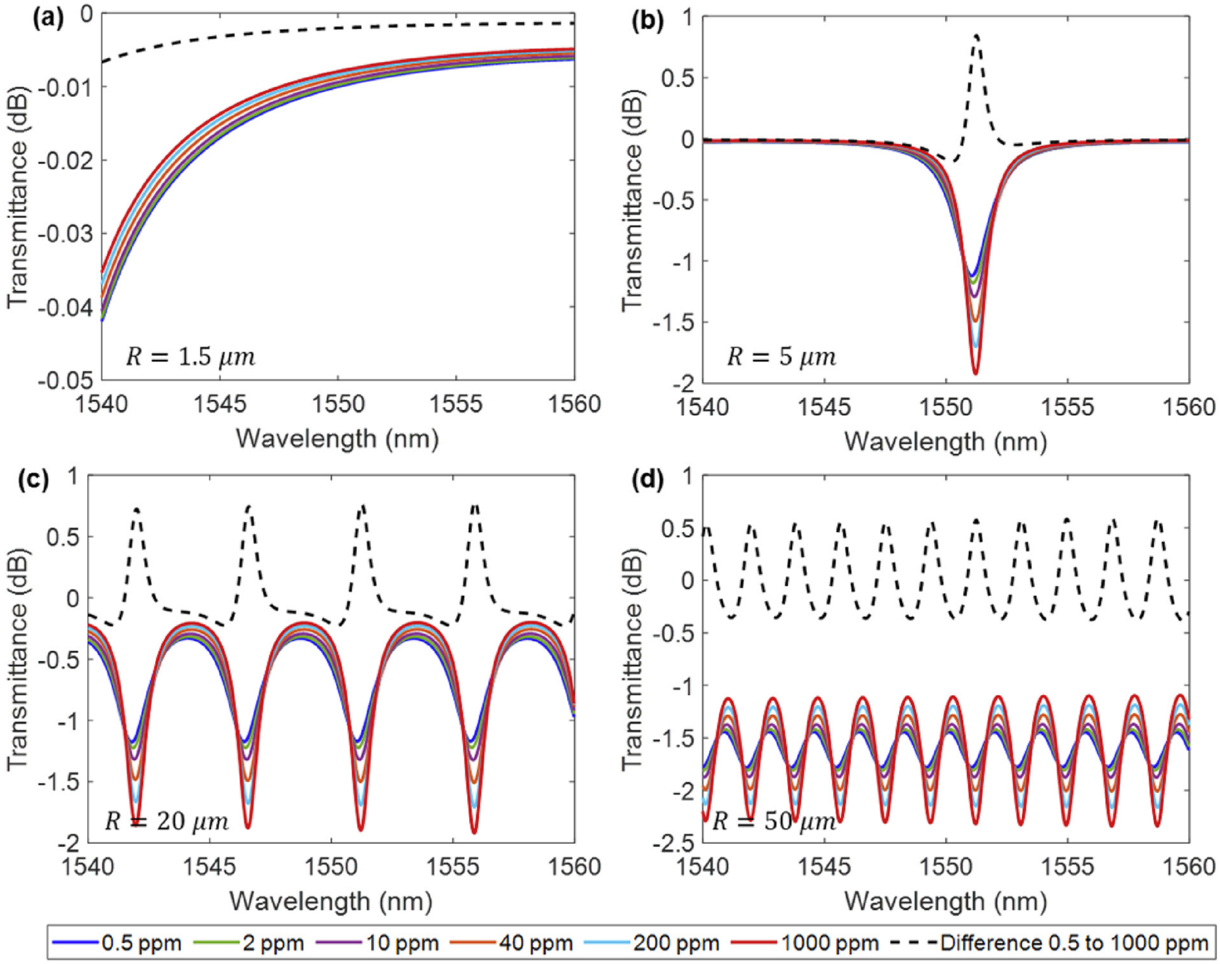

Fig. 8. Transmittance spectra for NH_3 concentrations of 0.5–1000 ppm versus wavelength for ring radius **(a)** 1.5 μm, **(b)** 5 μm, **(c)** 20 μm, and **(d)** 50 μm, under fundamental quasi-TE mode. The dashed black line in each figure represents the difference in transmittance between 0.5 and 1000 ppm.

The evaluated chemical potential μ_c of graphene corresponding to different ammonia gas concentration is shown in Fig. 2 (data extracted from Ref. [19]). Due to the intrinsic doping of CVD graphene as transferred employing typical methods, e.g., PMMA and wet etch methods, graphene's chemical potential under ambient conditions is not zero. This leads to graphene as-transferred being typically p-type. The ammonia gas molecules will also donate electrons to p-type graphene, thus altering its optical conductivity [24]. Although an external voltage can be applied to control graphene's chemical potential (in a gated configuration), this could lead to extra power consumption from the sensor.

Lumerical Eigenmode solutions [26] were employed to calculate the effective index of the waveguide in a broad wavelength range from 1540 nm to 1560 nm. The graphene layer is modeled as a 2D material with scattering rate 15 meV. The calculated complex effective index, $n = n_r + jn_i$, of fundamental quasi-TE and fundamental quasi-TM modes are shown in Fig. 3. The electric field intensity distributions and cross-sections of these two modes, at a wavelength of 1550 nm, are depicted in Fig. 4 under NH_3 concentration of 0.5 ppm and 1000 ppm.

The effective index shows dispersion of the waveguide covered with graphene as a function of wavelength. In Fig. 3 it is observed that the real part of the effective index of both TE and TM modes decreases with increase in wavelength. The real part of the effective index under TM mode is smaller than that for the TE mode. This can be understood from the TM mode field having stronger distributions in the low index regions (air and silicon dioxide), as observed in Fig. 4. The effective index, at 1550 nm, for the fundamental quasi-TE mode is 2.4203 + 0.0023i (0.5 ppm) and 2.4207 + 0.0013i (1000 ppm), and for the fundamental quasi-TM mode, the effective index at 1550 nm is 1.6110 + 0.0029*i* (0.5 ppm) and 1.6115 + 0.0017*i* (1000 ppm). The imaginary part of the effective index decreases with the increase of NH_3 gas concentration, which indicates that higher ammonia concentration can lead to less propagation loss of the guided waveguide mode.

The transmittance of the all-pass ring resonator is obtained by the following formula [27]:

$$T_n = \left(\frac{E_{output}}{E_{input}}\right)^2 = \frac{a^2 + r^2 - 2ar\cos\varphi}{1 + a^2r^2 - 2ar\cos\varphi}, \tag{5}$$

where r is the self-coupling coefficient of the straight waveguide, $a = a_0\exp(-2\pi n_i L/\lambda)$ is the single-pass amplitude transmission, which includes graphene attenuation, a_0 is the single-pass amplitude transmission of the ring resonator without graphene, $L = 2\pi R$ is the whole length of the ring waveguide, $\varphi = \beta L$ is the round-trip phase shift, and $\beta = 2\pi n_r/\lambda$ is the propagation constant of the mode.

The single-pass amplitude transmission a_0 of the ring resonator, without graphene, was simulated in Lumerical FDTD solutions [28] as a function of ring radius and extracted at a wavelength of 1550 nm. Fig. 5(a) shows the bending loss of one-quarter ring as a function of the bend radius for the two different propagation modes. The bending loss of the fundamental quasi-TE mode is relatively small compared to the fundamental quasi-TM mode; hence the fundamental quasi-TE mode has higher single pass amplitude transmission a_0. This can be attributed to high light confinement in the core of the fundamental quasi-TE mode. Besides, for both modes, the bending loss decreases as the bend radius

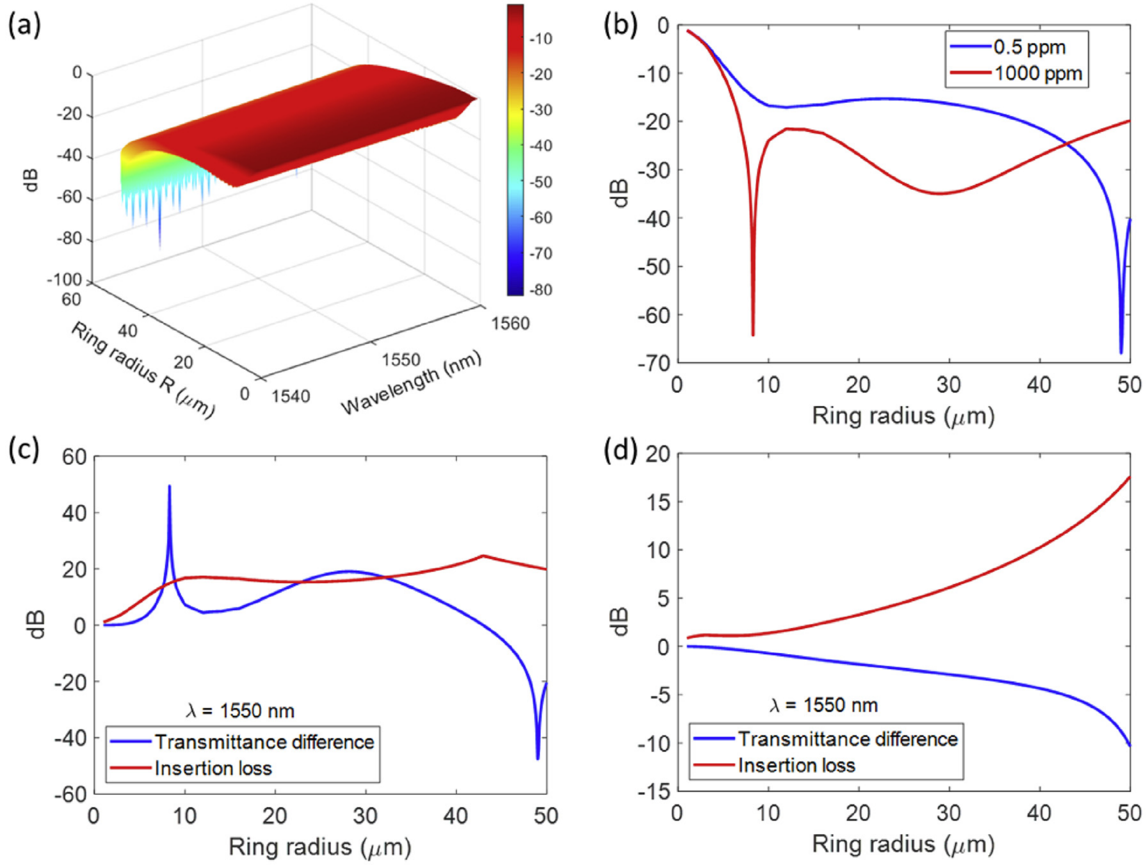

Fig. 9. (a) 3D plot of transmittance versus ring radius and wavelength for ammonia concentration of 0.5 ppm. **(b)** T_{min} versus ring radius for 0.5 ppm and 1000 ppm ammonia concentration. Transmittance difference and insertion loss as a function of ring radius under 0.5 ppm–1000 ppm NH_3 gas concentration **(c)** calculated from T_{min}, **(d)** calculated from T_{max}.

increases.

Lumerical 3D FDTD simulations [28] were performed to obtain the resonator's self-coupling coefficient without graphene for ring radius from 1 μm to 20 μm. The results were extracted at the wavelength of 1550 nm. Simulations were performed only up to 20 μm, since computational cost dramatically increases for larger radius. However, the self-coupling coefficient can be formulated analytically as discussed in Ref. [29]. From here it is observed that for the TE mode, the self-coupling coefficient at ring radius from 20 to 50 μm can be linearly extrapolated from the simulated data. For TM mode, it is observed that self-coupling quickly drops as R is increased. In this case, for ring radius from 20 μm to 50 μm, it can be derived mathematically from Ref. [29] that the self-coupling coefficient should approximately follow a square root dependence. By extrapolating the five last simulated points, a curve of the form $r = 0.9311 - 0.1247\sqrt{R}$ is employed to extrapolate the self-coupling coefficient for the fundamental quasi-TM mode.

As indicated by the results in Fig. 6(b), a larger ring radius leads to a stronger cross-coupling between the ring waveguide and the bus waveguide, hence a smaller value for the self-coupling coefficient, r [29]. Compared to the fundamental quasi-TE mode, the quasi-TM mode shows a stronger coupling between the straight waveguide and the ring waveguide, hence a weaker self-coupling. This can be explained from the perspective that the fundamental TE mode has a higher effective index than the fundamental TM mode, thus more energy is confined in the silicon core. While the exponential tail of the fundamental TM mode outside of the silicon core is longer and more light can be coupled into the ring waveguide.

Fig. 6 shows the calculated single-pass amplitude transmission of the ring waveguide, including graphene attenuation. Under fundamental quasi-TE mode, as depicted in Fig. 6(a), for ring radius smaller than 2 μm, bending loss dominates, while for ring radius greater than 2 μm, the loss is mainly dominated by graphene attenuation. As shown in Fig. 6(b), under the fundamental quasi-TM mode, the bending loss dominates until the ring radius reaches ~10 μm. As the ring radius further increases, the loss would be dominated by graphene attenuation. Moreover, both figures show a decrease in propagation loss of the guided modes with increasing ammonia gas concentration. Whereas for fundamental quasi-TE mode, self-coupling coefficient r is always larger than a, for fundamental quasi-TM mode, the condition $r = a$ could be satisfied for particular values R. This condition can lead to a critical coupling situation, causing a very large sensitivity of transmittance to ammonia concentration.

The transmittance $10\log_{10}(T_n)$, in dB, of the fundamental quasi-TE mode can be calculated from Eqn. (5). Fig. 7(a) presents a surface plot of transmittance versus ring radius and wavelength, for 0.5 ppm ammonia concentration. When varying the ring radius, the characteristic surface goes through several closely spaced minima and maxima, as highlighted in the detail depicted in Fig. 7(b). The minima and maxima satisfy the following conditions, respectively:

$$T_{min} = \frac{a^2 + r^2 - 2ar}{1 + a^2r^2 - 2ar}, \quad T_{max} = \frac{a^2 + r^2 + 2ar}{1 + a^2r^2 + 2ar}. \tag{6}$$

Fig. 7(c) shows the transmittance difference and insertion loss (in dB) calculated from the difference in T_{min} when varying the ammonia gas concentration from 0.5 ppm to 1000 ppm versus ring radius. We observe that: the larger the ring radius, the larger the loss. Furthermore, when analyzing the transmission difference, we observe that it exhibits a maxima at R ~5 μm. However, the observed differences are in all cases

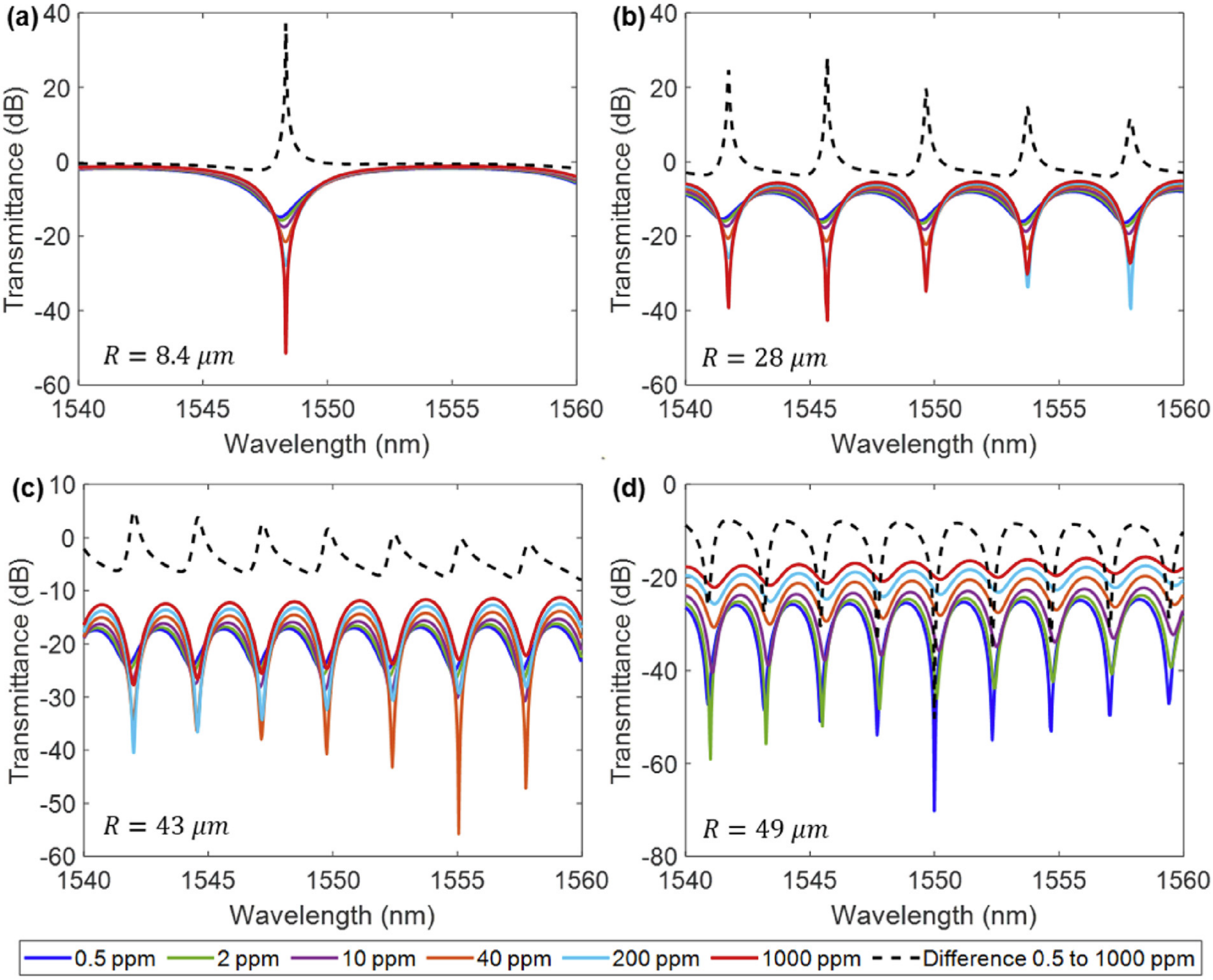

Fig. 10. Transmittance spectra for NH_3 concentrations of 0.5–1000 ppm versus wavelength for ring radius **(a)** 8.4 μm, **(b)** 28 μm, **(c)** 43 μm, and **(d)** 49 μm, under fundamental quasi-TM mode. The dashed black line in each figure represents the difference in transmittance between 0.5 and 1000 ppm.

$\ll$1 dB, which makes this not suitable as a detection platform. Fig. 7(d) shows the transmittance difference and insertion loss (in dB) calculated from the difference in T_{max} when varying the ammonia gas concentration from 0.5 ppm to 1000 ppm versus ring radius. A smaller transmission difference is observed than when tracking the T_{min}.

Depicted in Fig. 8(a-d) are transmittance plots at NH_3 concentrations of 0.5 and 1000 ppm, versus wavelength, for different ring radius: 1.5, 5, 20, and 50 μm. In agreement with the plots in Fig. 7, we observe maximum transmission modulation at the wavelengths when transmission level is close to a minimum. It is observed that the difference in transmittance maximizes for a particular ring radius, 5 μm, following the trends in Fig. 7(c).

A similar analysis was performed for quasi-TM mode. At this end, we present a surface plot of transmittance versus ring radius and wavelength, for 0.5 ppm, in Fig. 9(a). It is to notice a much larger variation in transmittance when altering ring radius than for the case of quasi-TE mode, which can be understood from a combination of a much smaller self-coupling coefficient, that is more light being coupled from the bus waveguide to the ring waveguide, as well as a particular attenuation characteristic, as depicted in Fig. 6(b), that could lead to critical coupling and very strong absorption of light by graphene. This is a phenomenon that can enhance the optical sensor sensitivity. Fig. 9(b) shows the transmittance levels T_{min}, calculated from Eqn. (6), versus ring radius for ammonia gas concentration of 0.5 ppm and 1000 ppm. We observe that when the ring radius is chosen to be ~8.4 μm, critical coupling is possible at 1000 ppm. In the other hand, if the ring radius is set to ~49 μm, critical coupling is possible at 0.5 ppm. Fig. 9(c) shows the transmittance difference and insertion loss (in dB) calculated from the difference in T_{min} when varying the ammonia gas concentration from 0.5 ppm to 1000 ppm versus ring radius. We again observe that the larger the ring radius, the larger the loss. In addition, we also notice, when analyzing the transmission difference, the presence of three "sweet spots" where maximum transmission difference, thus gas sensitivity, is possible. These occur for R = 8.4 μm, R ~28 μm, and R = 49 μm. Whereas the sweet spots at 8.4 and 49 μm are very narrow and have their origins on critical coupling being achieved at either 0.5 or 1000 ppm, the sweet spot at around 28 μm is broader. However, it is to note that non-monotonic dependences will be in this last case expected for transmission levels at intermediate ammonia concentrations. This is not desirable from a sensor perspective. Furthermore, whereas R = 8.4 μm could provide the best tradeoff between sensitivity and loss, the system's dynamic range in all cases will dictate the final sensor sensitivity. Assuming a dynamic range of 40 dB, performance will be similar for all these three cases. Fig. 9(d) shows the transmittance difference and insertion loss (in dB) calculated from the difference in T_{max} when varying the ammonia gas concentration from 0.5 ppm to 1000 ppm versus ring radius. Again, a smaller transmission difference is observed than when tracking T_{min}.

Depicted in Fig. 10(a-d) are transmittance plots versus wavelength for ammonia concentrations of 0.5 and 1000 ppm. These plots were generated for R = 8.4, 28, 43, and 49 μm, respectively. These cases correspond to exceptional points in Fig. 9(c), where difference in T_{min} maximizes (R = 8.4, 28, and 49 μm) or minimizes (R = 43 μm). It is observed that an inadequate ring choice, such as R = 43 μm, will not yield appreciable transmission modulation when the sensor is exposed to ammonia. However, through engineering the ring radius it is possible to attain a practical sensitivity level. Assuming the system dynamic range ~40 dB, both R = 8.4 μm and R ~28 μm could provide ~20 dB transmission modulation when ammonia gas concentration is varied from 0.5 to 1000 ppm. In both cases, the insertion loss is ~15 dB. A ring with R = 49 μm will provide a slightly smaller dynamic range, limited sensitivity, and a slighter larger insertion loss (~20 dB).

From the perspectives mentioned above, we identify that R = 8.4 μm could provide the best sensing performance, that is larger transmittance difference and lower insertion loss when varying ammonia concentration between 0.5 and 1000 ppm.

4. Conclusion

In summary, graphene-covered silicon microring resonators can achieve different transmittance sensitivity to ammonia depending on ring radius and mode excitation. The overall transmittance intensity difference, for the fundamental quasi-TE mode is less than 1 dB, independent of ring radius, when the ammonia gas concentration is varied from 0.5 to 1000 ppm. In the other hand, under fundamental quasi-TM mode, more than 20 dB transmittance intensity difference can be obtained by optimizing the ring radius. Moreover, the system dynamic range is crucial to, in practice, determine the maximum transmittance sensitivity.

Author statement

Wei Jia: Methodology, Investigation, Visualization, Writing - Review & Editing. **Apratim Majumder:** Validation. **Sourangsu Banerji:** Methodology. **Rajesh Menon:** Writing - Review & Editing. **Berardi Sensale-Rodriguez:** Conceptualization, Supervision, Writing - Review & Editing.

Declaration of competing interest

The authors declare that they have no known competing financial interests or personal relationships that could have appeared to influence the work reported in this paper.

Acknowledgements

This work was supported by the NSF award ECCS # 1936729.

References

[1] W. Bogaerts, P. Dumon, D.V. Thourhout, D. Taillaert, P. Jaenen, J. Wouters, et al., Compact wavelength-selective functions in silicon-on-insulator photonic wires, IEEE J. Sel. Top. Quant. Electron. 12 (2006) 1394–1401, https://doi.org/10.1109/jstqe.2006.884088.

[2] B. Ouyang, Y. Xing, W. Bogaerts, J. Caro, Silicon ring resonators with a free spectral range robust to fabrication variations, Opt. Express 27 (2019) 38698, https://doi.org/10.1364/oe.381643.

[3] A.W. Fang, R. Jones, H. Park, O. Cohen, O. Raday, M.J. Paniccia, et al., Integrated AlGaInAs-silicon evanescent race track laser and photodetector, Opt. Express 15 (2007) 2315, https://doi.org/10.1364/oe.15.002315.

[4] Q. Xu, B. Schmidt, S. Pradhan, M. Lipson, Micrometre-scale silicon electro-optic modulator, Nature 435 (2005) 325–327, https://doi.org/10.1038/nature03569.

[5] Q. Xu, S. Manipatruni, B. Schmidt, J. Shakya, M. Lipson, 12.5 Gbit/s carrier-injection-based silicon micro-ring silicon modulators, Opt. Express 15 (2007) 430, https://doi.org/10.1364/oe.15.000430.

[6] S. Xiao, M.H. Khan, H. Shen, M. Qi, A highly compact third-order silicon microring add-drop filter with a very large free spectral range, a flat passband and a low delay dispersion, Opt. Express 15 (2007) 14765, https://doi.org/10.1364/oe.15.014765.

[7] H. Shen, M.H. Khan, L. Fan, L. Zhao, Y. Xuan, J. Ouyang, et al., Eight-channel reconfigurable microring filters with tunable frequency, extinction ratio and bandwidth, Opt. Express 18 (2010) 18067, https://doi.org/10.1364/oe.18.018067.

[8] J.D. Orlet, R.C. Bailey, Silicon photonic microring resonator arrays as a universal detector for capillary electrophoresis, Anal. Chem. 92 (2019) 2331–2338, https://doi.org/10.1021/acs.analchem.9b05271.

[9] C. Qiu, J. Chen, Q. Xu, Ultraprecise measurement of resonance shift for sensing applications, Opt. Lett. 37 (2012) 5012, https://doi.org/10.1364/ol.37.005012.

[10] B. Sensale-Rodriguez, Graphene-based optoelectronics, J. Lightwave Technol. 33 (2015) 1100, https://doi.org/10.1109/JLT.2014.2373173.

[11] A. Vakil, N. Engheta, Transformation optics using graphene, Science 332 (2011) 1291–1294, https://doi.org/10.1126/science.1202691.

[12] F. Schedin, A.K. Geim, S.V. Morozov, E.W. Hill, P. Blake, M.I. Katsnelson, et al., Detection of individual gas molecules adsorbed on graphene, Nat. Mater. 6 (2007) 652–655, https://doi.org/10.1038/nmat1967.

[13] J.A. Lazaro, J. Gonzalez, J.A. Altabas, A. Lerin, Graphene silicon ring resonators for wavelength routers in photonic network-on-chip, in: 2015 17th International Conference on Transparent Optical Networks (ICTON), 2015, https://doi.org/10.1109/icton.2015.7193731.

[14] Y. Gao, W. Zhou, X. Sun, H.K. Tsang, C. Shu, Cavity-enhanced thermo-optic bistability and hysteresis in a graphene-on-Si_3N_4 ring resonator, Opt. Lett. 42 (2017) 1950, https://doi.org/10.1364/ol.42.001950.

[15] Y. Ding, X. Zhu, S. Xiao, H. Hu, L.H. Frandsen, N.A. Mortensen, et al., Effective electro-optical modulation with high extinction ratio by a graphene–silicon microring resonator, Nano Lett. 15 (2015) 4393–4400, https://doi.org/10.1021/acs.nanolett.5b00630.

[16] F. Zangeneh-Nejad, R. Safian, A graphene-based THz ring resonator for label-free sensing, IEEE Sensor. J. 16 (2016) 4338–4344, https://doi.org/10.1109/jsen.2016.2548784.

[17] L. Guo, Y.W. Hao, P.L. Li, et al., Improved NO_2 Gas sensing properties of graphene oxide reduced by two-beam-laser interference, Sci. Rep. 8 (2018) 4918, https://doi.org/10.1038/s41598-018-23091-1.

[18] N. Alzate-Carvajal, A. Luican-Mayer, Functionalized graphene surfaces for selective gas sensing, ACS Omega 5 (2020) 21320–21329, https://doi.org/10.1021/acsomega.0c02861.

[19] H. Kishikawa, M. Sato, N. Goto, S.-I. Yanagiya, T. Kaito, S.-K. Liaw, An optical ammonia gas sensor with adjustable sensitivity using a silicon microring resonator covered with monolayer graphene, Jpn. J. Appl. Phys. 58 (2019), https://doi.org/10.7567/1347-4065/ab24b7.

[20] S. Virji, J. Huang, R.B. Kaner, B.H. Weiller, Polyaniline nanofiber gas sensors: examination of response mechanisms, Nano Lett. 4 (2004) 491–496, https://doi.org/10.1021/nl035122e.

[21] J. Huang, J. Wang, C. Gu, K. Yu, F. Meng, J. Liu, A novel highly sensitive gas ionization sensor for ammonia detection, Sensor. Actuators A Phys. 150 (2009) 218–223, https://doi.org/10.1016/j.sna.2009.01.008.

[22] K. Besar, S. Yang, X. Guo, W. Huang, A.M. Rule, P.N. Breysse, et al., Printable ammonia sensor based on organic field effect transistor, Org. Electron. 15 (2014) 3221–3230, https://doi.org/10.1016/j.orgel.2014.08.023.

[23] T. Hao, K.S. Chiang, Graphene-based ammonia-gas sensor using in-fiber Mach-Zehnder interferometer, IEEE Photon. Technol. Lett. 29 (2017) 2035–2038, https://doi.org/10.1109/lpt.2017.2761981.

[24] F. Yavari, E. Castillo, H. Gullapalli, P.M. Ajayan, N. Koratkar, High sensitivity detection of NO_2 and i NH_3n air using chemical vapor deposition grown graphene, Appl. Phys. Lett. 100 (2012) 203120, https://doi.org/10.1063/1.4720074.

[25] G.W. Hanson, Dyadic Green's functions and guided surface waves for a surface conductivity model of graphene, J. Appl. Phys. 103 (2008), 064302, https://doi.org/10.1063/1.2891452.

[26] [Online]. Available: https://www.lumerical.com/products/mode/, 2020.

[27] W. Bogaerts, P.D. Heyn, T.V. Vaerenbergh, K.D. Vos, S.K. Selvaraja, T. Claes, P. Dumon, P. Bienstman, D.V. Thourhout, R. Baets, Silicon microring resonators, Laser Photon. Rev. 6 (2012) 47–73, https://doi.org/10.1002/lpor.201100017.

[28] [Online]. Available: https://www.lumerical.com/tcad-products/fdtd/, , 2020.

[29] M. Bahadori, K. Bergman, M. Nikdast, S. Rumley, L.Y. Dai, N. Janosik, et al., Design space exploration of microring resonators in silicon photonic interconnects: impact of the ring curvature, J. Lightwave Technol. 36 (2018) 2767–2782, https://doi.org/10.1109/jlt.2018.2821359.